Check for updates

Cyclic peptide-based shear-thinning and self-healing hydrogels as injectable nanotherapeutics

Fátima Santillán, [ID] [a] Yasmeen Shamiya, [ID] [a] Aishik Chakraborty, [ID] [b] Alap Ali Zahid, [ID] [c] Lorena Veliz, [ID] [a] François Lagugné-Labarthet, [ID] [a] Leonard G. Luyt [ID] [a,d,e] and Arghya Paul [ID] *[a,c]

An injectable cyclic peptide-based hydrogel (cpGel) governed by supramolecular interactions between cyclic octapeptide nanofibers and LAPONITE® was developed. We demonstrated its excellent injectability, elasticity, and self-healing properties through rheological analyses. Further, we showed that cpGel is cytocompatible and that vancomycin-loaded cpGel can effectively inhibit the growth of MRSA and *E. coli*.

1. Introduction

Hydrogels are soft materials consisting of three-dimensional (3D) networks of hydrophilic groups or chain segments capable of entrapping large quantities of water molecules without undergoing dissolution. These materials are mainly derived from polymers, polysaccharides, proteins, DNA, and small organic molecules such as peptides.[1–3] Moreover, these 3D networks are distinguished owing to their mechanical properties, high swelling capacity, and versatile functionality, making them suitable for various biomedical applications.[4–7] For example, their ability to closely mimic the extracellular matrix (ECM) allows them to be used as scaffolds that support cell adhesion, proliferation, and differentiation in tissue engineering, wound healing, and bone repair.[8] Further, injectable hydrogels have gained interest due to their self-healing properties, ability to adapt to any shape in real-time, and minimally invasive nature in surgery.[9,10] These injectable materials possess shear-thinning behavior that enables them to flow through narrow-gauge needles, then rapidly recover their 3D-network, making them suitable for applications in drug delivery and soft tissue engineering.[11,12]

Among different injectable hydrogels, supramolecular hydrogels formed through non-covalent interactions such as hydrogen bonds, electrostatic interactions, hydrophobic interactions, and π–π stacking are attractive because of their unique structures.[13–15] These interactions can enable self-healing behavior, tunable mechanical properties and stimuli responsiveness. Combining organic building blocks and inorganic nanomaterials is one advantageous way to fabricate supramolecular hydrogels.[16–18]

Peptides have been explored recently as organic building blocks for hydrogel formation because of their tunability and potential for bioactivity. Within the class of inorganic nanomaterials, the incorporation of nanosilicates (**nSi**, LAPONITE®) represents an attractive hydrogelator for its robust mechanical properties and ability to sustain drug release for biomedical applications.[16,19] For example, a recent study has shown the interaction between **nSi** and self-assembled linear peptide amphiphile nanostructures, resulted in hydrogels for potential applications in neovascularization and hierarchical mineralization.[16] However, cyclic peptides offer additional advantages compared to linear peptides. Their conformational rigidity and defined ring structure provide improved proteolytic stability, which can be critical in maintaining structural integrity in complex environments.[20–22] Therefore, these properties lead the cyclic peptides to a greater control over self-assembly with the ability to form nanostructures with well-defined internal surfaces and supramolecular architectures. Such well-defined architectures have been applied in previous studies involving molecular imaging, transmembrane channels, and drug delivery applications.[23–25] Overall, these features distinguish cyclic peptide-based architectures from many linear peptide assemblies and other soft hydrogelators, whose greater conformational flexibility often results in broader distributions in nanostructure size and morphology.[26] To the best of our knowledge, the interaction of **nSi** and cyclic peptide-based nanomaterials has not yet been explored.

[a]Department of Chemistry, Western University, 1151 Richmond St, London, Ontario, N6A 5B7, Canada. E-mail: arghya.paul@uwo.ca
[b]Chemical and Industrial Processes Engineering, Faculty of Engineering, Bahrain Polytechnic, Isa Town, The Kingdom of Bahrain
[c]Department of Chemical and Biochemical Engineering, Western University, 1151 Richmond St, London, Ontario, N6A 5B7, Canada
[d]Departments of Oncology and Medical Imaging, Western University, London, Ontario, N6A 3K7, Canada
[e]Verspeeten Family Cancer Centre, London Health Sciences Centre, 800 Commisioners Rd, London, Ontario, N6A 5W9, Canada

In this paper, we report on the development of a supramolecular hydrogel (**cpGel**) based on the non-covalent interactions of self-assembled organic cyclic octapeptide (**CP1**) nanofibers and inorganic nanosilicates (**nSi**) for antibacterial applications. Recently, the overuse of antibiotics has become a major concern and has severely burdened healthcare systems due to the emergence of antibiotic-resistant bacteria.

Sustaining the release of antibiotics can reduce their usage, offering a potential solution to antibiotic resistance.[27] Here, we quantified the sustained release of a model antibiotic, vancomycin, from **cpGel** and ensured its effectiveness against the growth of *Escherichia coli* (*E. coli*), *Staphylococcus aureus* (*S. aureus*), and methicillin-resistant *Staphylococcus aureus* (MRSA). To the extent of our knowledge, this report is the first instance of an injectable hydrogel platform based on the combination of cyclic peptide nanofibers and **nSi**. We envision that **cpGel** has the potential to be used in other related biomedical applications such as cancer therapy, wound healing, bone repair, and tissue engineering.

2. Results

CP1 nanofibers self-assemble from the elongation of CP1 nanotubes

As detailed in our previous work,[23] the cyclic octapeptide **CP1** cyclo(D-Leu-Lys-D-Leu-Tyr)$_2$ comprises alternating D- and L-amino acids, enabling the formation of elongated nanostructures in the form of nanotubes (Fig. S1). This is possible through the non-covalent interactions (hydrogen bonding) of the cyclic ring backbones, which form β-sheet structures, as well as minor contributions from the outer surface such as, π–π stacking of tyrosine rings. The self-assembly of **CP1** was performed through a pH-triggered process, wherein sodium hydroxide was gradually added to an acidified solution of **CP1** until reaching the desired pH (7.4). Under this pH condition, we expect the nanostructures to be mostly protonated due to the presence of the amino groups of lysine side chains. In our previous study, it was demonstrated that cyclic peptide concentrations ranging from 10–200 μM facilitate the formation of nanotubes. Here, the peptide concentrations used were higher (1.5% (w/v) ≡ 15 mM), enhancing the availability of the cyclic building blocks for the assembly process and promoting the elongation of nanotubes into nanofibers. To this end, it is hypothesized that this higher concentration promotes the lateral aggregation of the cyclic peptide nanotubes, generating nanofibers (Fig. 1a). This correlates well with previous studies where peptide nanotubes can form nanofibers.[28–30] Furthermore, the observed lateral aggregation may be related to hydrophobic interactions involving leucine residues. While this hypothesis was not directly investigated in the present work, previous studies have reported that leucine residues can support nanotube bundling,[31] consistent with hydrophobic "leucine zipper"-type interactions. Similar leucine-mediated interactions have also been utilized in the formation of cyclic peptide nanosheets.[32] Field emission scanning electron
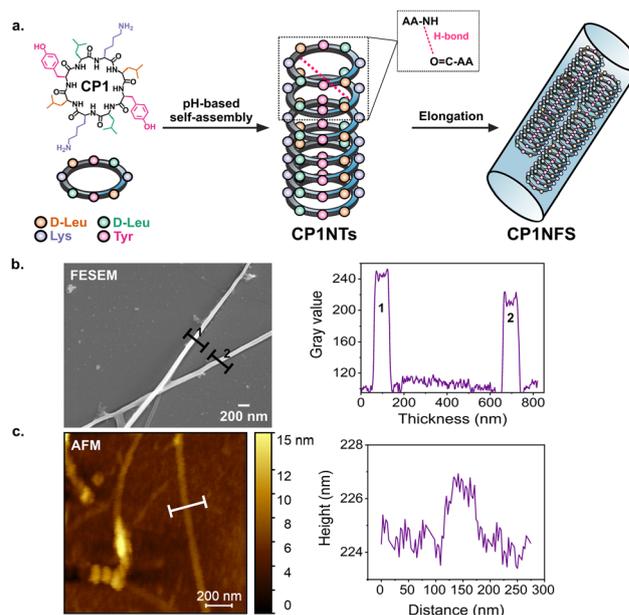

Fig. 1 Preparation and characterization of cyclic octapeptide (**CP1**) nanofibers. (a) Schematic outlining the formation of **CP1** nanofibers, AA: amino acid. (b) FESEM image of **CP1** nanofibers and plot profile showing their elongated structure with an estimated thickness of 73 nm. (c) AFM image of **CP1** nanofibers and height profile confirming their elongated structure and showing an estimated thickness value of 70 nm.

microscopy (FESEM) and atomic force microscopy (AFM) were used to evaluate the morphology of **CP1** nanofibers. FESEM micrographs confirmed the formation of elongated nanofibers with an estimated thickness of 73 nm and an average length of 2.1 ± 0.8 μm (Fig. 1, S2 and S3). AFM images corroborated the fabrication of nanofibers with an estimated thickness of 70 nm (Fig. 1c and S4), which aligns with the value determined from FESEM analysis. The reported thickness values support the statement that the cyclic peptide nanofibers are formed from elongated cyclic peptide nanotubes.

cpGel formed from electrostatic interactions between CP1 nanofibers and nSi

In this study, we aimed to fabricate an injectable hydrogel drug delivery platform using **CP1** nanofibers and **nSi**. At physiological pH, **CP1** nanofibers are positively charged (NH$_3^+$), which facilitates interactions with the negatively charged surface of **nSi**, leading to the formation of **cpGel** (Fig. 2a). FESEM confirmed the formation of **CP1** nanofibers, as shown in Fig. 2b. In the case of the hydrogel, FESEM micrographs showed **CP1** nanofibers surrounded by **nSi** (Fig. 2b, left and Fig. S5). The energy dispersive X-ray (EDX) spectrum of **cpGel** further confirmed the incorporation of **nSi** through the presence of Mg (Fig. S6), which serves as a distinguishing element between the materials forming the hydrogel structure. Fourier-transform infrared (FTIR) spectroscopy provided insight into the interactions between **nSi** and **CP1** nanofibers in the hydrogel (Table S1). As shown in Fig. 2c, **cpGel** displays the charac-
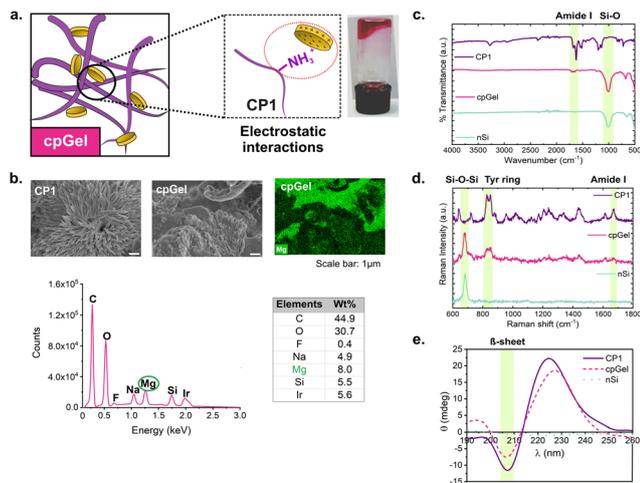
Fig. 2 Physico-chemical characterization of **cpGel**. (a) Schematic highlighting the electrostatic interactions between the protonated amino groups from **CP1** and the negative charge of **nSi** in **cpGel** (picture of **cpGel** vial). (b) FESEM images of **CP1** nanofibers and **cpGel** demonstrating the presence of the **CP1** nanofibers in the hydrogel. EDX spectrum and mapping of **cpGel** confirm the integration of **nSi** due to the presence of magnesium (selected representative element). (c) FTIR spectra (expanded image in Fig. S7), and (d) Raman spectra of **nSi**, **CP1** nanofibers, and **cpGel** supporting the electrostatic interactions between **CP1** nanofibers and **nSi**. (e) CD spectra of **nSi**, **CP1** nanofibers, and **cpGel** showing that the β-sheet conformation is maintained upon the addition of **nSi**.

teristic peaks of **nSi**[33,34] and **CP1** nanofibers. The characteristic peaks of **CP1** nanofibers seems less prominent in the FTIR spectrum of **cpGel** due to its lower relative content compared to **nSi** during hydrogel preparation (Fig. S7). Within this material, the Si–O–Si stretching peak is redshifted (1013 to 978 cm^{-1}), suggesting a possible change in the molecular environment, which may be attributed to electrostatic interactions between **nSi** and **CP1** nanofibers.[35,36] This shift may indicate alterations in the Si–O environment, possibly due to charge redistribution associated with the interactions with the protonated NH$_3^+$ of the peptide nanofibers. FTIR-active Si–O vibrational modes are known to be sensitive to changes in local chemical environment, including surface charge and variations in hydration and surface interactions, which could also contribute to this observed redshift.[37] Raman spectroscopy was further used to characterize the interactions within **cpGel** (Fig. 2d). All the peaks are summarized in Table S2. For **nSi**, the characteristic Si–O–Si vibration (682 cm^{-1}) is slightly redshifted in **cpGel** (679 cm^{-1}), suggesting a decreased vibrational frequency possibly caused by the electrostatic interactions with **CP1** nanofibers. In **cpGel**, the **nSi** characteristic peak and some peaks of **CP1** nanofibers were found, demonstrating the incorporation of both materials in the gel. The amide I band at 1671 cm^{-1} demonstrated the β-sheet conformation of the **CP1** nanofibers, which remains unchanged during hydrogel formation, as no band shift occurs. **CP1** nanofibers, **nSi**, and a representative **cpGel** sample were analyzed using circular dichroism (CD) spectroscopy (Fig. 2e). As expected, **nSi** displayed a flat line as a profile since it is not optically active and does not form secondary structures. The CD spectrum of **CP1** nanofibers showed a negative minimum at 208 nm, indicative of β-sheet-like structures. **cpGel** showed a similar CD profile to the **CP1** nanofibers, demonstrating that the conformation of these nanostructures is not disrupted with the incorporation of the **nSi** when forming the hydrogel network. Additionally, zeta potential was tested for **nSi**, **CP1** nanofibers, and **cpGel**. The zeta potential of **CP1** nanofibers was 17 ± 3 mV, as expected owing to the presence of protonated surface groups. In contrast, **nSi** exhibited a zeta potential of −45 ± 3 mV, which indicates the presence of negative charges on its surface.[19] For **cpGel**, the value was −30 ± 2 mV, which is indicative of the electrostatic interactions of positively charged groups of nanofibers and negatively charged groups of **nSi** (Fig. S8).

cpGel showed excellent shear-thinning and self-healing behavior

The structural properties of **cpGel** were evaluated using rheological measurements. 0% **cpGel** (0% **CP1**) was used as a control, this only contains 2.5% (w/v) **nSi** without the presence of cyclic peptide nanofibers. Amplitude sweep tests were carried out with 2.5% (w/v) **nSi** and varying concentrations of **CP1** (Fig. 3a and b). These tests showed increased elasticity with higher peptide concentrations, which is consistent with previous linear peptide-**nSi** systems.[16,38,39] We selected a final **CP1** concentration of 1.5% (w/v) for further experiments based on the elasticity. Additionally, when comparing to 2% (w/v) **CP1**, the G' values were similar, and we believe a high content of **CP1** would not add any rheological benefits (Fig. S9). From here on, all experiments were carried out using 2.5% (w/v) **nSi** and 1.5% (w/v) **CP1**. Fig. 3b also shows that our selected hydrogel displayed increased elasticity (higher storage modulus G') compared to the control group. Additionally, the values of G' of **cpGel** were greater than G'', confirming the formation of the hydrogel. Strain sweep tests further determined the linear viscoelastic region (LVR), with relative constant G' values up to 0.01% strain (Fig. S10). Frequency sweep tests (Fig. 3c) were then carried out within this LVR region, confirming the increased G' values in the hydrogel compared to the control group. Herein, this enhancement can be attributed to the interactions of the negatively charged surface of **nSi** and positively charged nanofibers that serve as physical crosslinking points within the hydrogel network.[19,40,41] Fig. 3c also showed that the values of G' and G'' were frequency-independent, indicating their high stability.[42]

Fig. 3d depicts the creep behavior over time for **cpGel** and the control group. The control undergoes significant deformation under stress and retains a greater amount of strain after unloading, while the hydrogel experiences less deformation and shows good recovery after removing the stress. In general, the hydrogel presents lower creep compliance, indicating that this material displays a high elastic behavior.[43,44]

After confirming the viscoelastic properties of the hydrogel, we tested its injectability. An injectable material presents a
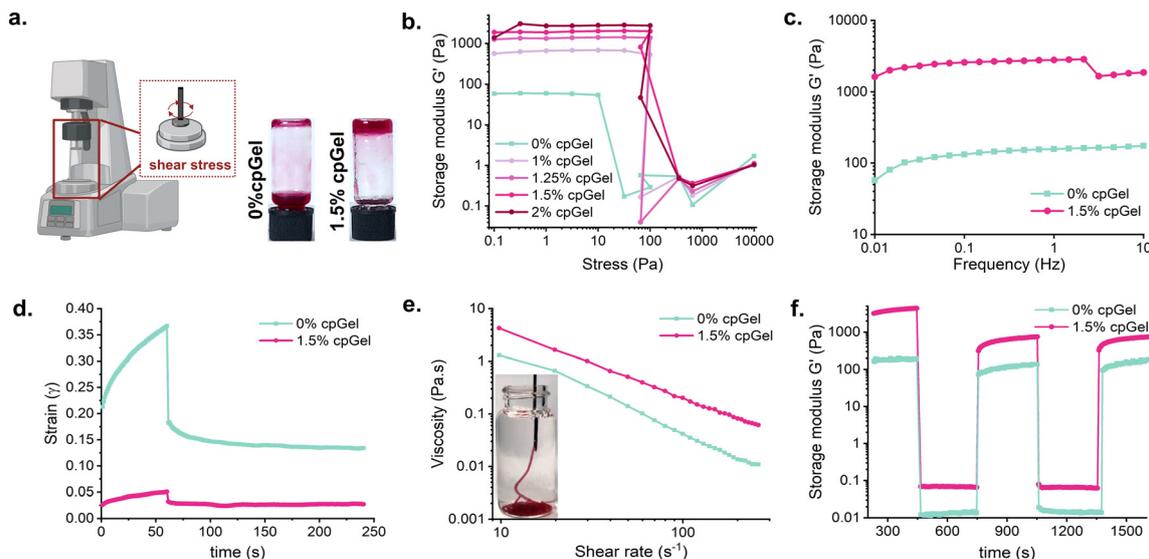
Fig. 3 Rheological characterization showing shear-thinning and self-healing properties of **cpGel**. (a) Schematic showing a rheometer, accompanied by the pictures of 0% **cpGel** (0% (w/v) **CP1**) and 1.5% **cpGel** (1.5% (w/v) **CP1**). (b) Amplitude sweep test of hydrogels containing 2.5% (w/v) **nSi** and different **CP1** concentrations, demonstrating an increase in elasticity with an increase of **CP1** concentration. (c) Frequency sweep test of 1.5% **cpGel** and a 0% **cpGel** as a control, showing an increase of the storage modulus. (d) Creep profiles demonstrating the high elastic behavior displayed by **cpGel**. (e) Viscosity profiles demonstrating the shear-thinning behavior of **cpGel** (inset: picture of **cpGel** being injected through a 27-gauge needle). (f) Recovery profiles of 0% **cpGel** and 1.5% **cpGel** demonstrating the recovery through different cycles of 0.01% strain and 1% strain.

shear-thinning behavior, which allows it to flow during injection and recover the 3D-structure once the mechanical load is removed. This was confirmed by passing the hydrogel through a 27-gauge needle, demonstrating its ease of injectability (Video S1). Viscosity tests (Fig. 3e) demonstrated the shear-thinning behavior of **cpGel**, where viscosity was reduced with increasing shear stress.[45] Additionally, injectable hydrogels present self-healing properties because of the presence of physical crosslinks, and this can be evaluated by assessing the recovery of the hydrogel through different cycles. We monitored the variation of G' over time cycles by adding and removing stress, as depicted in Fig. 3f. A complete recovery of the storage modulus was observed within seconds after removing 1% strain (Fig. S11). Furthermore, the stability of the gel over time was assessed by measuring the amplitude sweep of **cpGel** after 4 months resulting in no variation of the viscoelasticity (Fig. S12).

cpGel cytocompatibility with endothelial cells *in vitro*

We evaluated the cytotoxicity of **cpGel** by investigating the morphology of human umbilical vein endothelial cells (HUVECs) using live cell staining after 24 h and 72 h of treatment. As shown in Fig. 4a, no morphological differences were observed between the control and treated groups, indicating that the hydrogel exhibited no observable toxicity towards the cells. After evaluating the morphology, we aimed to quantitatively evaluate the cytotoxicity of **cpGel** with HUVECs. The hydrogel was incubated with HUVECs for 24 h, and the cytocompatibility was subsequently analyzed using flow cytometry and a commercial LIVE/DEAD staining kit. According to the ISO 10993-

5:2009 guidelines, a biomaterial can be considered cytocompatible if it maintains at least 70% cell viability compared with a negative control (cells only).[46–48] In our case, the negative control showed 92.47 ± 4.52% viable cells, whereas the positive control (cells subjected to heat) showed 42.97 ± 16.46%, and the hydrogel-treated group showed 86.67 ± 1.24%, as highlighted in Fig. 4b and c. Further, the results showed no significant differences between the control and the hydrogel-treated group. From these assays, we can conclude that **cpGel** is cytocompatible with endothelial cells and can be safely used for biomedical applications.

cpGel sustained the release of an antibiotic and retained its bioactivity

After demonstrating the safety of **cpGel**, we loaded a model antibiotic (vancomycin) into the hydrogel. Vancomycin is a glycopeptide antibiotic commonly used in the treatment of infections caused by Gram-positive bacteria (*S. aureus* and MRSA) and has been shown to work against Gram-negative bacteria (*E. coli*).[49–51] However, vancomycin has an *in vivo* half-life of approximately 4 to 6 h, requiring frequent administration. **cpGel** offers a platform for the sustained release of vancomycin.[52–54]

Before assessing the bioactivity of the vancomycin-loaded hydrogel, the cumulative release kinetics of vancomycin from hydrogels with varying concentrations of **CP1** were evaluated (Fig. 4d). We observed that hydrogels were able to sustain the release of vancomycin, possibly due to the electrostatic interactions of the negatively charged **nSi** and the slightly positively charged antibiotic. In addition, there could be some contri-
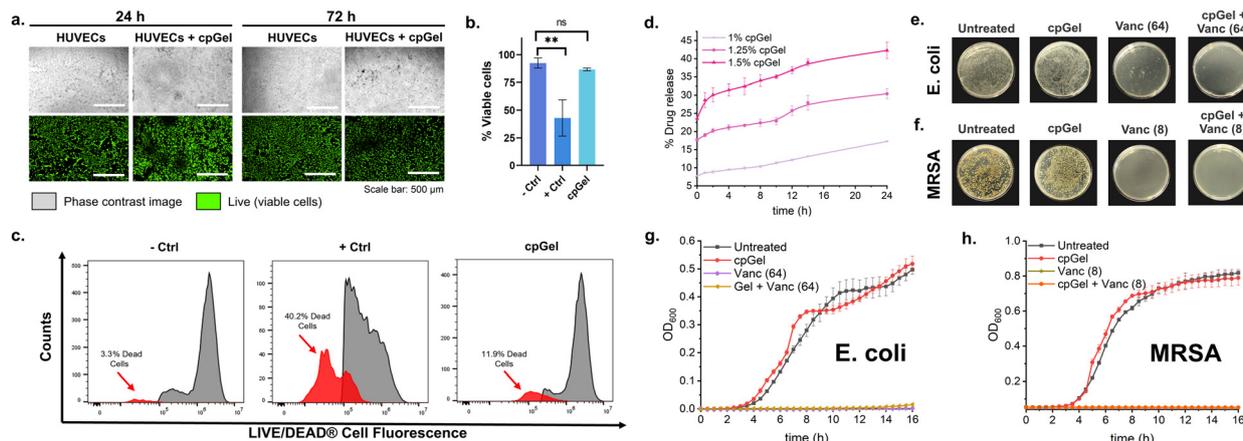
Fig. 4 Cytocompatibility and bioactivity of **cpGel** and vancomycin-loaded hydrogel. (a) Phase contrast and calcein fluorescence images of endothelial cells left untreated (HUVECs) and hydrogel-treated (HUVECs + **cpGel**) for 24 h and 72 h, scale bar = 500 μm. (b) Graph showing the percentage of cell viability determined by flow cytometry ($n = 3$), wherein the hydrogel-treated group displayed 86.67 ± 1.24% cell viability. This percentage of viability is in accordance with ISO 10993-5:2009. +Ctrl refers to cells exposed to heat, whereas −Ctrl refers to cells left untreated. Statistical significance was determined by ordinary one-way ANOVA corrected using the Dunnet method (**$p < 0.01$). (c) Representative samples showing the amounts of dead cells using flow cytometry of −Ctrl (3.3%), +Ctrl (40.2%), and **cpGel** (11.9%). (d) Vancomycin release using hydrogels with different content of **CP1**. Increasing concentrations of **CP1** show higher antibiotic release, possibly due to repulsive interactions between **CP1** nanofibers and the antibiotic. (e) Pictures of *E. coli* and (f) MRSA colonies after 16 h ($n = 3$). (g) Effects of hydrogel-released vancomycin and free vancomycin on the growth of *E. coli* and (h) MRSA up to 16 h. In both cases, the plots show the bioactivity of the drug is maintained after being released from the hydrogel. For figures (e) to (h), the concentration in brackets is expressed in μg mL^{-1}.

bution of hydrogen bonding between amino groups in vancomycin and hydroxyl groups on the surface of **CP1** nanofibers. For a better understanding of these interactions, Raman spectra of vancomycin (Vanc), vancomycin-loaded **CP1** nanofibers (Vanc-**CP1**), and vancomycin-loaded hydrogel (Vanc-**cpGel**) are described in Fig. S13 and Table S3. Overall, some characteristic peaks of the drug are observed in the spectra of Vanc-**CP1** and Vanc-**cpGel**, although some signals overlap. For instance, the peak at 831 cm^{-1} of Vanc, assigned to an out-of-plane ring breathing vibration, overlaps with the Tyr-ring breathing vibration in the other spectra. Additionally, the Amide III vibration in vancomycin (1236 cm^{-1}) is slightly downshifted in Vanc-**CP1** (1241 cm^{-1}) and Vanc-**cpGel** (1238 cm^{-1}). These changes in the spectra can be due to modifications in the local environment, since the amide III bonds are sensitive to hydrogen bonding.[55] The amide I at 1236 cm^{-1}, is slightly shifted in the other spectra. Since this peak can be used as indicative of the β-sheets formation, we also assessed the CD spectra of these materials (Fig. S14). The vancomycin sample underwent the same pH-assembly method, and its CD spectrum showed the absence of β-sheets, as expected. For the Vanc-**CP1** and Vanc-**cpGel**, the minimum at 208 nm (mentioned in Fig. 2e) is not affected by the incorporation of the drug, indicating that the drug does not disrupt the self-assembly process. We also assessed the stability of the **cpGel** after vancomycin incorporation in its network and no variations was found in the elastic behavior (Fig. S15, left). Also, FESEM image of Vanc-**cpGel** demonstrated there is no variation in the morphology of the hydrogel (Fig. S15, right), herein we found some crystals that were not present in the **cpGel** sample, this may indicate that the crystals correspond the vancomycin.

The formulation containing 1.5% (w/v) **CP1** showed a higher release percentage compared to formulations with lower concentrations of **CP1**. This higher release may be due to the repulsive interactions between the increased positive charges from amine groups of **CP1** nanofibers and the protonated amine group within the sugar unit in the vancomycin. The vancomycin release kinetics from the formulation containing 1.5% (w/v) **CP1** showed 42.25 ± 2.24% release of the drug after 24 h using UV-Vis spectroscopy. This result was further verified with a representative sample using high-performance liquid chromatography (HPLC), which showed 40.57% release after 24 h (Fig. S16). This drug release behavior is very consistent with a previous study reporting the release of ≈40% from a peptide-based hydrogelator.[56] To model the release of vancomycin from **cpGel**, the release data by UV-Vis was fit to the Korsmeyer–Peppas model (Table S4). The numeric coefficient of this model (n) was lower than 0.45 ($n = 0.1192$) indicating that the release is *via* diffusion. This is consistent with a previous report of vancomycin release from peptide vehicles.[57]

Next, we assessed the bioactivity of the vancomycin-loaded **cpGel** by monitoring the bacterial growth up to 16 h after exposure to *E. coli*, *S. aureus*, and MRSA. We treated all the samples with hydrogel-released vancomycin and free vancomycin (control). The minimum inhibitory concentration (MIC) of vancomycin was 64 μg mL^{-1} for *E. coli* and 8 μg mL^{-1} for MRSA.[58] Overall, the hydrogel-released vancomycin exhibited comparable efficiency to free vancomycin, demonstrating the successful release of different concentrations of the drug and retention of bioactivity (Fig. 4g, h, S17, and S18). Fig. 4e and f present images of the bacterial plates, corroborating the effective antibacterial release properties of **cpGel**.

3. Conclusions

We have successfully developed an injectable supramolecular hydrogel capable of sustaining the release of vancomycin. **cpGel** was fabricated by combining cyclic octapeptide (**CP1**) nanofibers and inorganic nanosilicates (**nSi**). The formation of **CP1** nanofibers was confirmed by FESEM and AFM, which exhibited an estimated thickness of 73 and 70 nm, respectively. The surface of these nanofibers is protonated under physiological pH, providing a means for interaction with the negatively charged surface of **nSi** to form **cpGel**. This resulting hydrogel displayed shear-thinning and self-healing properties. Moreover, **cpGel** demonstrated cytocompatibility with endothelial cells according to acceptable ISO standards. Finally, vancomycin was used as a model drug to be loaded into **cpGel** and demonstrated its efficacy as a drug release platform. It was further corroborated that the drug maintained its activity after release from **cpGel** against Gram-positive and Gram-negative bacteria, including MRSA. Overall, it is envisioned the potential use of this injectable supramolecular hydrogel platform for various biomedical applications.

Author contributions

Fátima Santillán: conceptualization, experiments, methodology, original draft, review and editing of manuscript. Yasmeen Shamiya: experiments, editing of manuscript. Aishik Chakraborty: rheology, editing of manuscript. Alap A. Zahid: flow cytometry, discussions. Lorena Veliz: Raman and AFM experiments and discussions. François Lagugné-Labarthet: Raman and AFM discussions. Leonard G. Luyt: conceptualization, funding, supervision, and editing the manuscript. Arghya Paul: conceptualization, funding, supervision, and editing the manuscript.

Conflicts of interest

There are no conflicts to declare.

Data availability

The data supporting this article have been included as part of the supplementary information (SI). Supplementary information is available. See DOI: https://doi.org/10.1039/d5bm01544h.

Acknowledgements

References

1 S. Aleid, M. Wu, R. Li, W. Wang, C. Zhang, L. Zhang and P. Wang, *ACS Mater. Lett.*, 2022, **4**, 511–520.

2 Z. An, L. Zhang, Y. Liu, H. Zhao, Y. Zhang, Y. Cao, Y. Zhang and R. Pei, *Biomater. Sci.*, 2021, **10**, 100–113.

3 C. Wu, X. Wang, Y. Shi, B. Wang, W. Xue and Y. Zhang, *Biomater. Sci.*, 2020, **8**, 6190–6203.

4 W. Gong, H. Huang, X. Wang, W. He, Y. Hou and J. Hu, *Biomater. Sci.*, 2022, **10**, 6836–6849.

5 Y. Shamiya, A. Chakraborty, A. A. Zahid, N. Bainbridge, J. Guan, B. Feng, D. Pjontek, S. Chakrabarti and A. Paul, *Commun. Mater.*, 2024, **5**, 197.

6 A. Chakraborty, S. Pacelli, S. Alexander, S. Huayamares, Z. Rosenkrans, F. E. Vergel, Y. Wu, A. Chakravorty and A. Paul, *Mol. Pharmaceutics*, 2023, **20**, 767–774.

7 S. Basu, A.-R. Alkiswani, S. Pacelli and A. Paul, *ACS Appl. Mater. Interfaces*, 2019, **11**, 34621–34633.

8 L. L. Panigrahi, S. Satpathy, P. Samal, S. Shekhar, S. K. Prusty and M. Arakha, *Nanoscale Adv.*, 2025, 7, 7209–7225.

9 S. Ishikawa, Y. Yoshikawa, H. Kamata, U. Chung and T. Sakai, *ACS Appl. Mater. Interfaces*, 2022, **14**, 35444–35453.

10 F. Zehtabi, P. Ispas-Szabo, D. Djerir, L. Sivakumaran, B. Annabi, G. Soulez, M. A. Mateescu and S. Lerouge, *Acta Biomater.*, 2017, **64**, 94–105.

11 L. Zhao, L. Niu, H. Liang, H. Tan, C. Liu and F. Zhu, *ACS Appl. Mater. Interfaces*, 2017, **9**, 37563–37574.

12 C. Ding, L. Zhao, F. Liu, J. Cheng, J. Gu, S. Dan, C. Liu, X. Qu and Z. Yang, *Biomacromolecules*, 2010, **11**, 1043–1051.

13 S. H. Jeong, M. Kim, T. Y. Kim, H. Kim, J. H. Ju and S. K. Hahn, *ACS Appl. Bio Mater.*, 2020, **3**, 5040–5047.

14 C. F. V. Sousa, J. Borges and J. F. Mano, *Biomater. Sci.*, 2025, **13**, 3617–3632.

15 F. Ettoumi, H. Huang, Y. Xu, L. Wang, Q. Ru, Y. Hu, L. Zou and Z. Luo, *Food Hydrocolloids*, 2024, **154**, 110108.

16 B. O. Okesola, A. K. Mendoza-Martinez, G. Cidonio, B. Derkus, D. K. Boccorh, D. Osuna de la Peña, S. Elsharkawy, Y. Wu, J. I. Dawson, A. W. Wark, D. Knani, D. J. Adams, R. O. C. Oreffo and A. Mata, *ACS Nano*, 2021, **15**, 11202–11217.

17 P. Keravitayanan and A. K. Gaharwar, *Acta Biomater.*, 2015, **26**, 34–44.

18 A. Nojoomi, E. Tamjid, A. Simchi, S. Bonakdar and P. Stroeve, *Int. J. Polym. Mater. Polym. Biomater.*, 2017, **66**, 105–114.

19 S. Basu, S. Pacelli, Y. Feng, Q. Lu, J. Wang and A. Paul, *ACS Nano*, 2018, **12**, 9866–9880.

20 J. D. Hartgerink, T. D. Clark and M. R. Ghadiri, *Chem. – Eur. J.*, 1998, **4**, 1367–1372.

21 N. Li, S. Qiu, Y. Fang, J. Wu and Q. Li, *Biology*, 2021, **10**, 688.

22 H. L. Sham, C. A. Rempel, H. Stein and J. Cohen, *J. Chem. Soc., Chem. Commun.*, 1990, 666–667.

23 F. Santillán, C. L. Charron, B. C. Galarreta and L. G. Luyt, *Nanoscale*, 2024, **16**, 22001–22010.

24 S. C. Larnaudie, J. Sanchis, T.-H. Nguyen, R. Peltier, S. Catrouillet, J. C. Brendel, C. J. H. Porter, K. A. Jolliffe and S. Perrier, *Biomaterials*, 2018, **178**, 570–582.

25 M. Calvelo, C. I. Lynch, J. R. Granja, M. S. P. Sansom and R. Garcia-Fandiño, *ACS Nano*, 2021, **15**, 7053–7064.

26 Q. Song, Z. Cheng, M. Kariuki, S. C. L. Hall, S. K. Hill, J. Y. Rho and S. Perrier, *Chem. Rev.*, 2021, **121**, 13936–13995.

27 D. Cocker, G. Birgand, N. Zhu, J. Rodriguez-Manzano, R. Ahmad, K. Jambo, A. S. Levin and A. Holmes, *Nat. Rev. Microbiol.*, 2024, **22**, 636–649.

28 A. Bayón-Fernández, A. Méndez-Ardoy, C. Alvarez-Lorenzo, J. R. Granja and J. Montenegro, *J. Mater. Chem. B*, 2023, **11**, 606–617.

29 H. Shaikh, J. Y. Rho, L. J. Macdougall, P. Gurnani, A. M. Lunn, J. Yang, S. Huband, E. D. H. Mansfield, R. Peltier and S. Perrier, *Chem. – Eur. J.*, 2018, **24**, 19066–19074.

30 A. Dasgupta, J. H. Mondal and D. Das, *RSC Adv.*, 2013, **3**, 9117.

31 J. D. Hartgerink, J. R. Granja, R. A. Milligan and M. R. Ghadiri, *J. Am. Chem. Soc.*, 1996, **118**, 43–50.

32 I. Insua and J. Montenegro, *J. Am. Chem. Soc.*, 2020, **142**, 300–307.

33 A. Ayub, Z. A. Raza, M. I. Majeed, M. R. Tariq and A. Irfan, *Int. J. Biol. Macromol.*, 2020, **163**, 603–617.

34 S. Snigdha, N. Kalarikkal, S. Thomas and E. K. Radhakrishnan, *Bull. Mater. Sci.*, 2021, **44**, 107.

35 B. Behera and P. K. Das, *J. Phys. Chem. A*, 2018, **122**, 4481–4489.

36 Y. Liu, H. Meng, S. Konst, R. Sarmiento, R. Rajachar and B. P. Lee, *ACS Appl. Mater. Interfaces*, 2014, **6**, 16982–16992.

37 T. Lagström, T. A. Gmür, L. Quaroni, A. Goel and M. A. Brown, *Langmuir*, 2015, **31**, 3621–3626.

38 Y. Hu, Y. Wang, Y. Liu, J. Dai, J. Wang and C. Ju, *Colloids Surf., B*, 2025, **253**, 114745.

39 T. De Serres-Bérard, T. B. Becher, C. B. Braga, C. Ornelas and F. Berthod, *ACS Appl. Polym. Mater.*, 2020, **2**, 5790–5797.

40 S. Jatav and Y. M. Joshi, *Appl. Clay Sci.*, 2014, **97–98**, 72–77.

41 P. Kensbock, D. E. Demco, S. Singh, K. Rahimi, R. Fechete, A. Walther, A. M. Schmidt and M. Möller, *Langmuir*, 2017, **33**, 66–74.

42 C. C. S. Boulet, A. Brown, C. Formstone and D. G. A. L. Aarts, *Rheol. Acta*, 2022, **61**, 811–825.

43 T. C. Brito-Oliveira, I. C. F. Moraes, S. C. Pinho and O. H. Campanella, *Food Hydrocolloids*, 2022, **123**, 107183.

44 J. Li, H. Liu, C. Wang and G. Huang, *RSC Adv.*, 2017, **7**, 35311–35319.

45 M. H. Chen, L. L. Wang, J. J. Chung, Y.-H. Kim, P. Atluri and J. A. Burdick, *ACS Biomater. Sci. Eng.*, 2017, **3**, 3146–3160.

46 ISO 10993-5:2009(en), Biological evaluation of medical devices—Part 5: Tests for in vitro cytotoxicity, https://www.iso.org/obp/ui/en/#iso:std:iso:10993:-5:ed-3:v1:en, accessed May 20, 2025.

47 K. Klimek, S. Terpilowska, A. Michalak, R. Bernacki, A. Nurzynska, M. Cucchiarini, M. Tarczynska, K. Gaweda, S. Głuszek and G. Ginalska, *ACS Biomater. Sci. Eng.*, 2025, **11**, 845–865.

48 M. R. Romano, M. Ferrara, C. Gatto, B. Ferrari, L. Giurgola and J. D'Amato Tóthová, *Transl. Vis. Sci. Technol.*, 2019, **8**, 24.

49 W. Jame, B. Basgut and A. Abdi, *PLoS One*, 2021, **16**, e0260539.

50 Q. Liu, D. He, L. Wang, Y. Wu, X. Liu, Y. Yang, Z. Chen, Z. Dong, Y. Luo and Y. Song, *Antibiotics*, 2024, **13**, 866.

51 C.-E. Choi, A. Chakraborty, H. Adzija, Y. Shamiya, K. Hijazi, A. Coyle, A. Rizkalla, D. W. Holdsworth and A. Paul, *Gels*, 2023, **9**, 923.

52 C. T. Gustafson, F. Boakye-Agyeman, C. L. Brinkman, J. M. Reid, R. Patel, Z. Bajzer, M. Dadsetan and M. J. Yaszemski, *PLoS One*, 2016, **11**, e0146401.

53 J. Hoque, B. Bhattacharjee, R. G. Prakash, K. Paramanandham and J. Haldar, *Biomacromolecules*, 2018, **19**, 267–278.

54 D.-V. Nguyen, Y. Yuan, M. Kukumberg, L. Wang, S. H. Lim, A. M. Hassanbhai, M. Chong, T. Kofidis, E. C. K. Tan, D. Seliktar, L. Kang and A. J. Rufaihah, *Biomater. Adv.*, 2024, **161**, 213896.

55 S. A. Oladepo, K. Xiong, Z. Hong, S. A. Asher, J. Handen and I. K. Lednev, *Chem. Rev.*, 2012, **112**, 2604–2628.

56 A. Baral, S. Roy, A. Dehsorkhi, I. W. Hamley, S. Mohapatra, S. Ghosh and A. Banerjee, *Langmuir*, 2014, **30**, 929–936.

57 J. Hwang, H. Huang, M. O. Sullivan and K. L. Kiick, *Mol. Pharmaceutics*, 2023, **20**, 1696–1708.

58 J. Huang, A. Chakraborty, Y. Shamiya, W. Luo, A. A. Zahid and A. Paul, *NPJ Biomed. Innov.*, 2025, **2**, 29.